Journal of Petroleum Science and Engineering 208 (2022) 109502

Contents lists available at ScienceDirect

Journal of Petroleum Science and Engineering

journal homepage: www.elsevier.com/locate/petrol

Fundamental constraints of lithologically-controlled fault networks on gas migration and accumulation for fractured carbonates in the western Sichuan Basin, China

Lin Zhang [a], Zonghu Liao [a,*], Ke Long [b], Brett M. Carpenter [c], Huayao Zou [a], Fang Hao [d]

[a] State Key Laboratory of Petroleum Resources and Prospecting, China University of Petroleum (Beijing), Beijing, 102249, China
[b] Exploration and Development Institute, SINOPEC Southwest Oil and Gas Branch Company, Chengdu, Sichuan, 610041, China
[c] School of Geosciences, University of Oklahoma, Norman, OK, 73019, USA
[d] School of Geosciences, China University of Petroleum (East China), Qingdao, Shandong, 266555, China

ARTICLE INFO

Keywords:
Subsurface fault networks
Leikoupo dolostone
3D seismic attributes
Subsurface anticline
Gas migration

ABSTRACT

The structure of subsurface fault networks, which has a significant effect on hydrocarbon migration, is inherently difficult to recognize and map. 3D seismic surveys provide an opportunity to map the fault system within a carbonate reservoir of Xinchang in the western Sichuan Basin, China. We calculated attributes from the seismic reflection data that covers an area of 1330 km^2, including variance, edge detection, dip-magnitude and dip azimuth. We focused on the Triassic Leikoupo Formation of dolostone, at ~6 km depth, adjacent to the Longmen Shan thrusting range. The mapped attributes display (1) a primary network of faults in an orthogonal pattern in the anticline, striking East-West and North-South, and (2) a secondary, conjugate fault set in the fold limb, striking Northeast and Northwest with a length range of 1–10 km. The latter set of conjugate faults are confined to a 300 m-thick layer of dolostone, diminishing into underlaying unit of anhydrite. We envision that the conjugate fault networks and associated fractures enhance gas charging and reflect a model of self-sourced migration and accumulation in the Leikoupo Formation. These results are significant for sweet-spot evaluation of carbonate reservoirs in the Sichuan Basin, and provide insights for understanding the migration of subsurface fluids.

1. Introduction

The presence of fault networks and associated fractures in carbonate and evaporate lithologies, controls the subsurface location and migration of fluid in hydrocarbon reservoirs (Chilingarian et al., 1992; Ameen, 2003; Lunn et al., 2008; Bhattacharya and Verma, 2019), as well as potential earthquakes that often nucleate or propagate through these sequences (Barchi, 2002; Miller et al., 2004; De Paola et al., 2008). Fault networks are basin-scale connected discontinuities with fractures or joints in the rock due to brittle deformation of the stratigraphy (Segall and Paola, 1983; Kim et al., 2003; Flodin and Aydin, 2004; Crider and Peacock, 2004). Previous analyses of the geometries and interrelationships of the carbonate- and evaporite-hosted faults are mostly based on outcrop observations and field measurements (Caine et al., 1996; De Paola et al., 2008; Putz-Perrier and Sanderson, 2010). The air photo of fold-related fault/joints on Teton Anticline in Montana provides a particularly clear illustration of a fault network in the field (Fig. 1, Stearns, 1968; Burberry et al., 2019). A regular array of faults/joints within the rock is also reported as a brittle structure network within Cretaceous limestones in Big Bend National Park in Texas (Harmon Maher, 2000, a web reference). The fault network, and associated fractures, are important for many reasons including as reservoirs and conduits for fluids moving through rock bodies (Chester et al., 1993; Caine et al., 1996; Chester and Chester, 1998). However, the structure of fault networks in the subsurface, that may behave as a conduit system to control the fluid flow, are inherently difficult to characterize and remain enigmatic due to lack of data.

In recent decades, seismic data acquisition has been applied to unlock hydrocarbon exploration potential (Nixon et al., 2014; Bhattacharya and Verma, 2019; Eng and Tsuji, 2019). More recently, seismic attributes computed from the seismic survey illustrate the potential to characterize fault structures in the subsurface at a depth range of 0–10 km (Gao, 2013; Wilson et al., 2015; Liao et al., 2017, 2019). Seismic attributes are based on neighborhood analysis of the seismic signal

* Corresponding author.
E-mail address: zong@cup.edu.cn (Z. Liao).

https://doi.org/10.1016/j.petrol.2021.109502
Received 8 March 2021; Received in revised form 10 July 2021; Accepted 14 September 2021
Available online 22 September 2021

corresponding to the discontinuities, which is helpful in identifying subtle features that are difficult to interpret directly on the seismic cube (Chopra and Marfurt, 2007). Many attributes have been investigated to detect faults in the basins, including semblance (Marfurt et al., 1998), coherence (Marfurt et al., 1999; Wu, 2017), curvature (Roberts, 2001; Al-Dossary and Marfurt, 2006), dip-magnitude and dip-azimuth (Chopra and Marfurt, 2007). Iacopini and Butler (2011) determined the structure and distribution of deformation in submarine thrust structures by using attributes of coherence, curvatures, and spectral decomposition. Liao et al. (2017, 2019) analyzed a km-scale subsurface strike-slip fault in Oklahoma by using attributes of coherences, curvatures, dip-magnitude and dip-azimuth. The degree to which useful fault information can be extracted depends on the seismic resolution and the natural complexity of the structures.

In this study, seismic attributes were applied to investigate the fault networks in the Xinchang gas reservoir that is composed of carbonates and evaporates, in the western Sichuan Basin, China. The attributes of variance, edge detection, dip-magnitude and dip-azimuth are used to better reveal the spatial distribution of faults as a system. We then discuss the implications of the results and suggest the structural controls on the gas reservoir at the basin scale.

2. Geological setting

The Sichuan Basin is one of the most natural gas-rich basins in China (Dai et al., 2014; Li et al., 2015; Wang et al., 2015; He et al., 2019). The western Sichuan depression is a northeast-trending foreland basin that formed during the late Triassic Indosinian Orogeny (Liu et al., 2010; Li et al., 2003). The basin lies along the northwest Yangze Block, which has experienced two complex tectono-sedimentary stages of evolution during the Phanerozoic eon (Guo et al., 2014; Zhang and Zheng, 2013): (a) a passive margin, with extension, accompanied with the sedimentation of marine carbonate and clastic sequences from the Ediacaran through middle Triassic, and (b) a foreland basin as a result of compression and uplift, with a fill of continental siliciclastic sediments from the Late Triassic to the Quaternary of less than 10-km thickness (Li et al., 1995). The western depression is bounded by two seismically-active mountainous ranges, the Longmen Shan in the west and the Longquan Shan in the east. Our study area is located in the middle part of western Sichuan depression, adjacent to the multi-million-populated Chengdu city (Fig. 2a and b). Since the Middle Triassic, the study area is under the nappe compression by the Himalaya orogeny in the west (Wang et al., 2014; Li et al., 2012; Dai et al., 2013).

The identified strata from bottom to up include: the Precambrian crystalline basement, Cambrian Formation of shale, Permian Formation of Liangshan (P_2l) mudstone and limestone, Qixia (P_2q) limestone, Maokou (P_2m) limestone, Longtan (P_3l) limestone, shale and intercalated with coal seams, and Changxing (P_3ch) limestone and shale, Triassic Formation of Feixianguan (T_1f) shale, Jialingjiang (T_1j) anhydrite, Leikoupo (T_2l) dolostone, limestone and anhydrite, Ma'antang (T_3m) mudstone and limestone, Xiaotangzi (T_3xt) and Xujiahe (T_3x) shale and sandstone, Jurassic and Quaternary Formation of sandstone, mud-shale and conglomerate, and the Leikoupo Formation is generally divided into four members based on lithological characteristics. We focus on the marine strata of carbonates and evaporates from Permian to Triassic periods: the organic-rich source rocks include Permian Longtan (P_3l) and Maokuo (P_2m) limestone, and Triassic Leikoupo Formation (T_2l) dolostone; the main reservoir rock is dolostone in the Triassic Lei-4-3 submember ($T_2l_4^3$); the caprock is low-permeability terrigenous mudstone deposited in the Upper Triassic. The target layer is the Triassic Leikoupo Formation dolostone, at an average depth of ~6000 m, which sits on a 500-m-thick ductile layer of anhydrite in the Lower Triassic Jialingjiang Formation (T_1j; Sun et al., 2020) (Fig. 2c).

3. Methodology of seismic attributes

Detailed interpretation of seismic attributes along horizon slices, strata slices or seismic profiles revealed more changes in subsurface structural characterization than observable from the seismic amplitude data alone (Bahorich and Farmer, 1995; Weimer and Davis, 1996; Sarkar et al., 2010). In this study, in order to analyze the structure of the fault networks in the subsurface, we used a set of high-resolution 3D seismic data (Fig. 2b) collected during 2010–2012. It was processed using a method of post-stack time migration with a dominant frequency of 22 Hz. The seismic data were recorded with two-way travel time to depth, which covers an area of ~1330 km^2, at a depth range from ~2000 ms to ~4000 ms. We computed volumetric seismic attributes including dip-magnitude, dip-azimuth, variance, and edge detection.

The dip is the angle measured between the horizontal plane and the targeted layer, which is often expressed as dip magnitude (Chopra and Marfurt, 2007). Dip azimuth is the strike measured in the direction of maximum downward dip. The dip angle can be calculated from the apparent angle on the inline (longitudinal line) and crossline (transverse line). Assuming that the apparent angle in the direction of inline is θi and in the direction of crossline is θc, then θi and θc are related to the dip angle (θ) as follows:

$$\theta = (\theta i + \theta c)^{1/2} \quad (1)$$

θi and θc are related to the dip azimuth (ϕ) as follows:

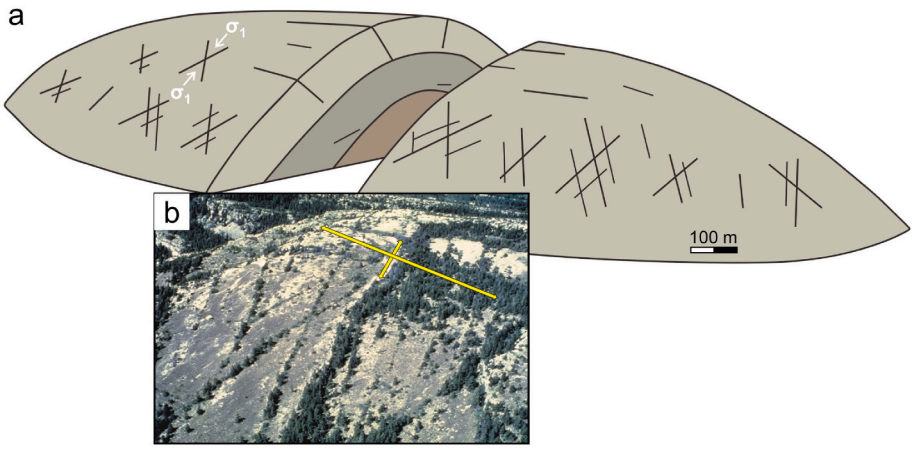

Fig. 1. (a) Conceptual fold model showing a set of conjugate shear fractures and their associated fractures (modified from Stearns, 1968; Burberry et al., 2019). (b) Air photo of tectonic fold-related faults/fractures on Teton Anticline, Sawtooth Mountains, W. Montana. Trees growing in the fractures are about 10 m tall. (Photo courtesy of Ron Nelson).

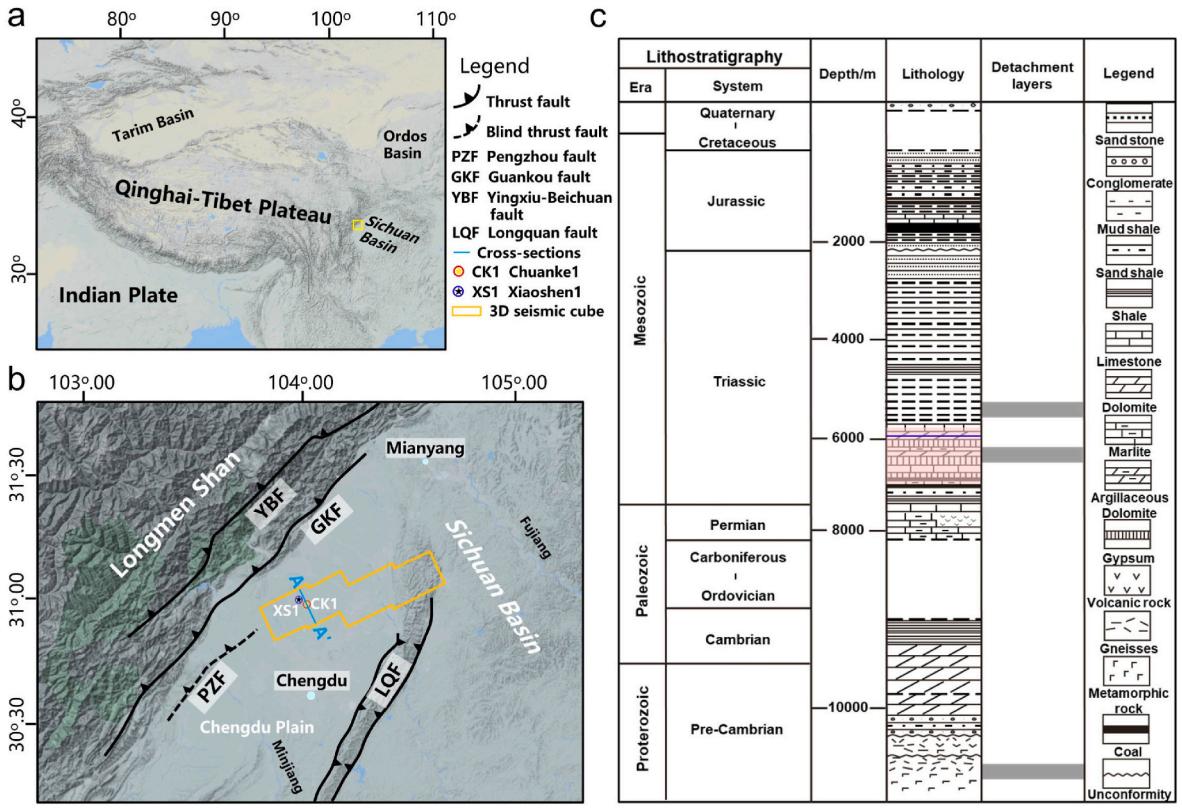

Fig. 2. General region of the study area (a) and the tectonic setting of the study area (b). Map (b) displays: 1) the main faults, Yingxiu-Beichuan (YB), Guankou (GK), Pengzhou (PZ), Longquan (LQ); 2) the study area; 3) seismic profile A-A'; 4) drilling well, CK1 and XS1. (c) The sedimentary stratigraphy of the Xingchang area (modified after Lu et al., 2019). Shaded red zone depicting the strata from T_1j to T_2l Formation; blue line depicting the layer of dolostone in Fig. 3. (For interpretation of the references to colour in this figure legend, the reader is referred to the Web version of this article.)

$$\phi = atan(\theta i, \theta c) \tag{2}$$

Variance is one of the seismic coherence attributes, which is a measure of discontinuities (D, Eq. (3)) of waveforms and traces. High values indicate discontinuities due to strata deformation e.g., faults, or fracturing. Determinations of variance change are based on amplitude, frequency and phase, depending on the acoustic-impedance contrast (Chopra and Marfurt, 2007). It is defined as:

$$D^2 = \frac{\sum_i^n (x_i - \overline{x})^2}{n} \tag{3}$$

in which, x indicates the energy value of a sample point, $\overline{x}$ indicating the mean energy value of the sample points, n indicating the number of the samples.

The edge detection method of Luo et al., (1996) (SEG' 1996 Expanded Abstracts) measures the change of adjacent traces (Carter and Lines, 2001). With a signal A on the target trace and signal B on an adjacent trace, we can calculate the difference between the two traces by the following equation:

$$d = \| A - B \| / (\| A \| + \| B \|) \tag{4}$$

in which a high value indicates discontinuities of subsurface structure.

In addition to four geometrical seismic attributes, core samples from one gas drilling well, CK1, were collected, which has been drilled through Cenozoic, Cretaceous, Jurassic, Middle-Upper Triassic layers and terminated at the Lower Triassic Jialingjiang Formation. Thin sections of dolostone from Triassic Leikoupo Formation were analyzed.

4. Results

4.1. Fault networks within dolostone by seismic attributes

The variance attribute is mapped in Fig. 3a for a volume reflector of the Leikoupo Formation in Middle Triassic. This map displays two superposed structural features (Fig. 3a): First, a fault network developed in the dolostone layer, with general faults marked by black arrows. This is a primary fault network that has two sets of faults in an orthogonal relationship, one set striking East-West, and the other set striking North-South. The lengths of North-South faults range from 5 km to tens of kms with variable spacing that averages ~3 km. Second, adjacent to the well CK1, there is a secondary set of conjugate faults. The conjugate faults are also fold zones in this region (Figs. 3a and 4a). These secondary faults strike Northeast-Southwest (45° in Figs. 3a and 4a, e, f) and Northwest-Southeast (Figs. 3a and 4a, e, f). There is a total of 16 subfaults constrained by the fold limb, with an intersection angle of about 70° (Fig. 4e). The average spacing of the secondary fault network is estimated to be ~0.9-km.

Edge-detection maps (Figs. 3b and 4b) reveal abundant information: (1) several major fault damage zones (horizontal white arrows) striking East-West; (2) two North-South fault zones; (3) a damage zone composed of the small conjugate faults (inside the blue box) striking North-East. The high production well, CK1, is located on the anticline top next to the conjugate fault network that dominates the south limb of the anticline. These conjugate fault networks are also distinguishable by attributes of dip-magnitude and dip azimuth (Fig. 3c and d, 4c, d). On the other hand, the north fold-limb is also damaged as shown by a red-yellow stripe in the edge-detection map, however, without a seismically-detectable fault network in the attribute maps, e.g., variance map. The conjugate pattern of the secondary fault network detected in this study

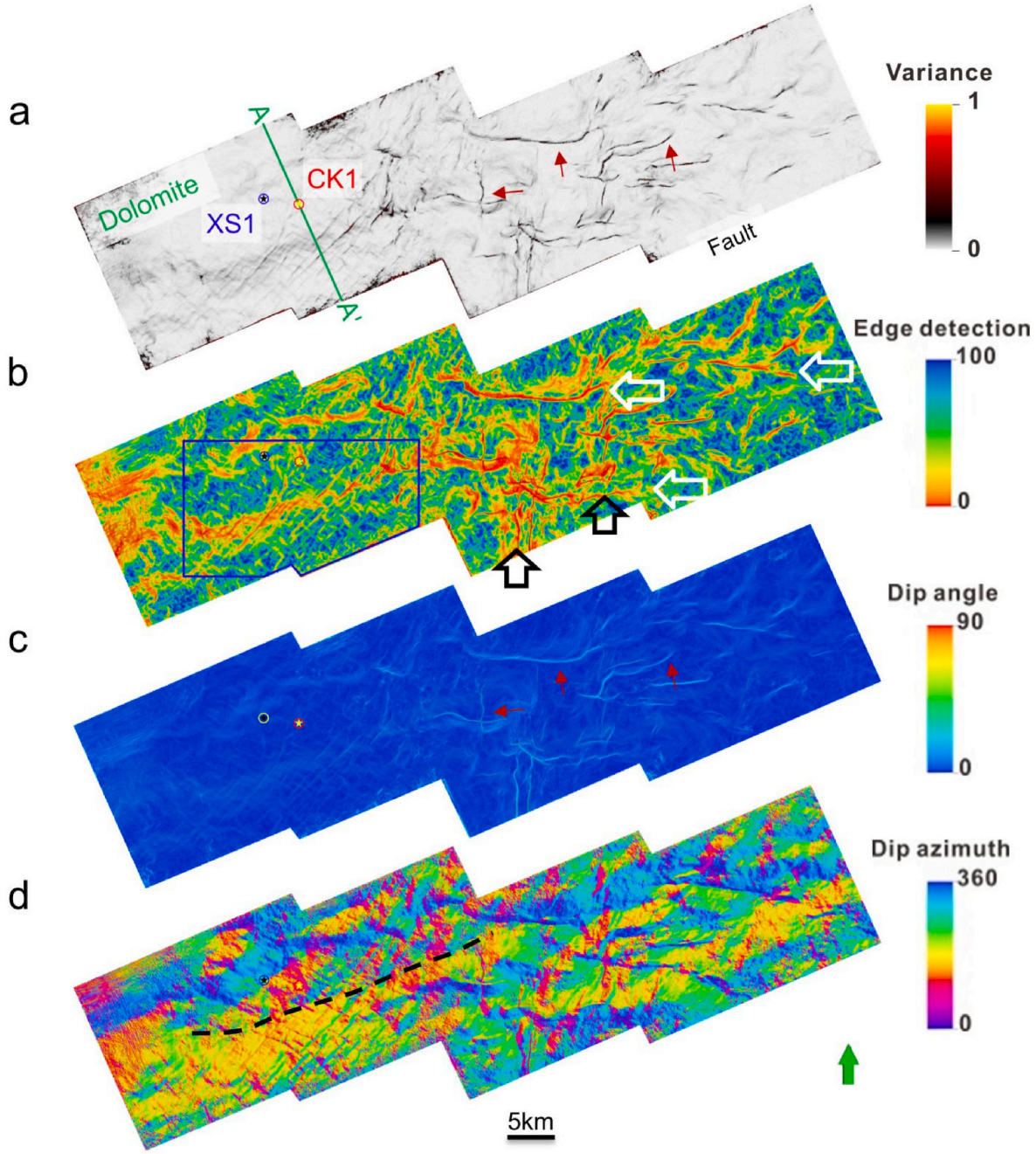

Fig. 3. (a) Strata slice (at layer of dolostone) from volumetric seismic attributes of variance, (b) edge detection, (c) dip, and (d) dip azimuth. A-A': seismic profile; CK1, XS1: drilling wells; solid blue box: the area of conjugate fault networks; arrows: major fault damage zones; dashed line: fold axis. (For interpretation of the references to colour in this figure legend, the reader is referred to the Web version of this article.)

compares well with the field observations of joints in the Teton Anticline in Montana (Stearns, 1968; Bergbauer and Pollard, 2004; Burberry et al., 2019, Fig. 1).

To identify the fold axis of the fold that may control the conjugate fault network, the dip-azimuth attribute is calculated (Fig. 3d) to show the strike of the seismic reflector (Chopra and Marfurt, 2007). Our observations from the dip-azimuth map suggests a fold axis (black dashed line) that divides the fold into north limb (blue patches in Fig. 3d) and south limb (yellow patches in Fig. 3d).

4.2. Fault networks and folds

Complementary profiles of seismic amplitude and variance (Fig. 5) are selected along line AA' (defined in Fig. 2b) that crosses both well CK1 and the conjugate fault network. These sections reveal the anticline within the Middle Triassic Leikoupo Formation of dolostone, with the underlaying Lower Triassic Jialingjiang Formation of anhydrite. The amplitude signals exhibit a strongly-disturbed texture around the anhydrite layer, which is enhanced by the attribute of variance in shaded red zone (Fig. 5b). The anticline is comprised of several "Y" patterns indicative of reverse faults and their associated damage zones. However, the set of conjugate fault networks cannot be distinguished based on the profiles of seismic amplitude and attribute. Apparently, the vertical lengths of the conjugate fault networks are constrained by the thickness of the dolostone formation that is less than 300 m. The internal character of the damaged dolostone is discussed below via observations

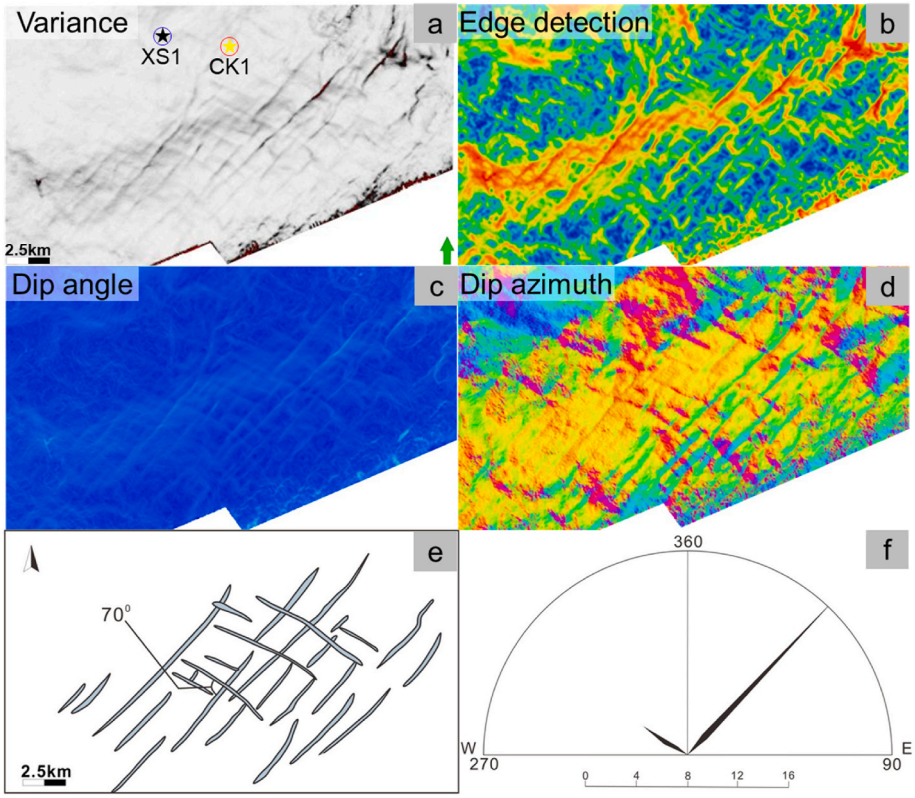

Fig. 4. (a–d) The conjugate fault networks depiction using volumetric seismic attributes (curvature, edge detection, dip/dip azimuth). Map location is shown in Fig. 3b. (e) Sketch of conjugate fault networks. (f) Rose diagram of the orientations of the conjugate fault networks.

of thin sections.

Based on the above four seismic attributes (Figs. 3 and 4), we recognize two sets of fault networks. One is the primary fault network that displays relatively large deformation intensity and rotation; the other set is the secondary conjugate fault network that is developed on the fold limb with a relatively smaller scale. The latter set of conjugate faults is associated with folding and are important for evaluation of reservoir conduits, which is the focus in this study.

4.3. Fractures within dolostone

The orthogonal geometry of the primary fault network and secondary fault network appear to be particularly developed in regions of relative compression characterized by appearance of anticlinal fold and twisting or rotation of the primary faults (e.g., Stearns, 1968; Bergbauer and Pollard, 2004; Ghosh and Mitra, 2009; Watkins et al., 2015). The formation of an anticline and reverse faults usually occurs with small-scale natural fractures in the brittle dolostone that have undergone compression. Based on the observations of the drilling core samples and thin sections, we found that two groups of the fractures: (1) large-fractures with apertures >0.1 mm, and (2) small-fractures with apertures <0.1 mm (Laubach, 2003; Anders et al., 2014). The large-fractures in cores and thin sections present average density of 1.4–2.2/mm (Fig. 6). These fractures are often filled with calcite with high dip-angles (50-90°). The small-fractures extend linearly with low dip-angles (0-30°, Fig. 6b–h). Some of them branch into several small sub-fractures. However, the wide-occurrence of low dip-angle fractures may be linked to overpressure of critically stressed fractures during natural resource extraction and storage (Fig. 6e–h e.g., Ellsworth, 2013; Luo et al., 2020). The length of these two sets of fractures ranges from tens of microns to centimeters, forming a fracture network. The above analysis shows that the Triassic Leikoupo dolostone has a large number of fractures in addition to faults, consisted as the potential migration conduits in the subsurface.

5. Discussion

5.1. Implication of the fault networks in hydrocarbon accumulation models

The previous results of reservoir characterization from the western Sichuan Basin show the Leikoupo Formation rock is composed of powder-crystalline dolostone and dolomicrite (He et al., 2019; Xiao et al., 2019). 32% of samples show moderate porosity of 2%–5% while the permeability is low with a peak value 0.002–0.25 md (He et al., 2019). The observation of low permeability is not easily reconciled with the primary discoveries of exploration targets in this region (Tian et al., 2018; Chen et al., 2018). If the fault networks and associated fractures represent optimum conduits for Leikoupo Formation reservoirs, we would expect that the conjugate fault networks control the hydrocarbon accumulation and is the key for understanding the hydrocarbon accumulations in strongly heterogeneous and low permeable rocks. Here we speculate on implication of fault networks for explaining the hydrocarbon accumulation models in Xinchang reservoir and their limitations.

(1). **Model 1: Self-sourced migration and accumulation.** If Xinchang reservoir is the self-sourced migration and accumulation model (Fig. 7a and b), its inherited structural high in the anticlinal is favorable for hydrocarbon accumulation, and the conjugate fault networks and associated fractures might be the controlling conduits facilitating gas charging into its current trap. In this view, faults and fractures near the anticline would be sealed by mudstone above and anhydrite below as a lithological-controlled network. It is capable of carrying gas over a large area of 200 km^2. As the principal source rocks are inferred within the Leikoupo Formation itself (Yang, 2016; Long et al., 2019), the

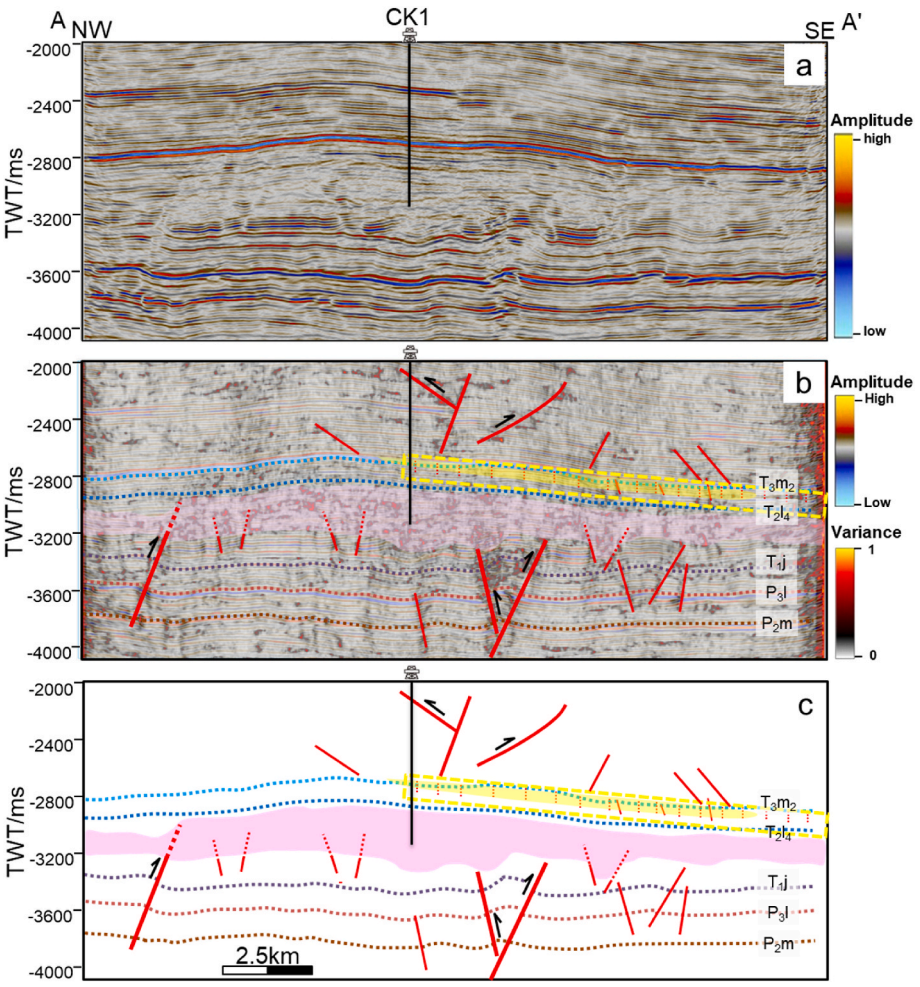

Fig. 5. Structural and geological interpretation of seismic profile A-A′, The (b, c) are the interpretations of the seismic profile (a). Dotted yellow rectangle depicts the zone of conjugate fault networks; thickness of the red line depicts the fault scale; shaded red zone depicts dolostone, limestone and anhydrite accumulation region. (For interpretation of the references to colour in this figure legend, the reader is referred to the Web version of this article.)

proximal hydrocarbon supply is possible when the fault-fracture networks developed into their current configurations. A further evolving of the structure would create clustering of faults that allow gas to escape from the trap. This self-sourced model has the advantage of being consistent with our observations of the fault networks, and the fractures show the significant potential as pathways.

(2). **Model 2: Long-range upward migration and accumulation.** The long-range upward migration model (Fig. 7c) would connect the current dolomitic reservoir with a source that is likely to be Permian ~7500 m (based on Li et al. (2016)' velocity model) below. For this to be so, the model requires large-scale faults for hydrocarbon migration across the impermeable, 500-m-thick anhydrite layer. This hypothesis would not apply as the Xinchang structure formed with only an anticline and fault networks that diminished into the underlaying anhydrite. However, because of seismic resolution limitations, thin faults that partially propagate into anhydrite as secondary pathway would be possible.

(3). **Model 3: Vertical downward migration and accumulation.** Based on the previous studies on the origination of natural gas in the Leikoupo Formation and fault-scale identification, most of the source rock comes from Leikoupo Formation and overlying Ma'antang Formation in this model (Fig. 7d). If the Ma'antang Formation acted as source rock, the vertical downward migration model would play a role in the gas accumulation. He et al. (2019) analyzed the burial history of the strata since Middle Triassic at the CK1 well and suggested that the period of natural gas generation was mainly from Lower Jurassic to Paleogene (~160-60 Ma, Fig. 8). The formation of fault networks was closely related with the uplift of the Longmen Shan range in the Late Miocene (Li et al., 2012; Dai et al., 2013; Wang et al., 2014), which was later than natural gas generation and would modify the Xinchang reservoir subsequently (Fig. 8). The tilted fold limb would enhance the downward migration of gas from Ma'antang source rock into the fracture system. Indeed, in this model the fault networks and associated fractures would behave as primary pathway for both resource sequences in above and below.

5.2. *Exploration plays in Xinchang*

In this study, we propose that conjugate fault networks in the Xinchang fold limb would behave as Model 1 described above, although downward migration is a complementary possibility. In the model of self-sourced migration and accumulation, hydrocarbons accumulate in a stratigraphically-controlled reservoir in the Xinchang. As the aforementioned migration model indicates, the distribution of faults and fractures would determine the favorable areas for investigation. The well of CK1 is a highly productive well near the anticlinal axis, with a cumulative gas production that exceeds 1.2×10^8 m^3 (Xu et al., 2011, 2013; Xie, 2015). In contrast, another well, XS1, located 4 km to the east of CK1 in the same anticlinal high area, is proven as a dry well without

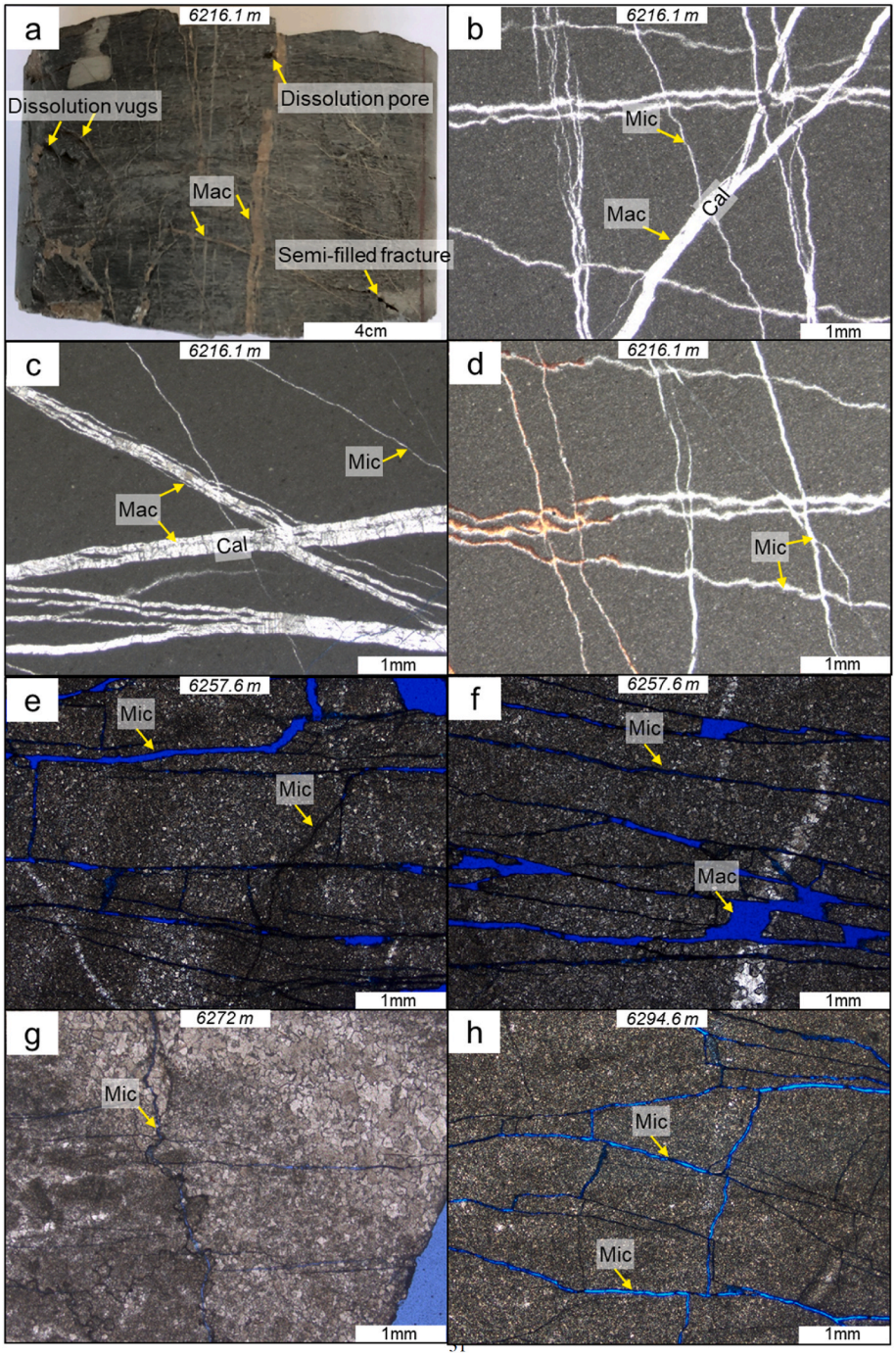

Fig. 6. Geological characteristics of calcite-filled/unfilled fractures system within the Middle Triassic Leikoupo Formation. (a) Core photo of macro-tectonic fractures partially filled by calcite from the CK1 well. (b–d) Thin sections of macro-tectonic fractures and micro-tectonic fractures filled with calcite from the CK1 well. (e–h) Thin sections of macro-tectonic fractures and micro-tectonic fractures from the LS1 well (13.7 km west of Xinchang block). Photomicrographs (b–h) were taken under plane-polarized light. Abbreviations: Mac (Macro-fracture), Mic (Micro-fracture), Cal (Calcite).

production. The likely reason is that the well of CK1 is inside the conjugate fault networks, where the development of fault networks provide systematic pathways for natural gas migration and the accumulation of commercial gas. As to the well of XS1, the location that is far away from such fault networks would tend to prohibit any potential accumulation (Figs. 3 and 7).

Previous studies on faults as migration conduits are mainly focused on seismic-scale single fault or regional fault systems (Billi et al., 2003; Karlsen and Skeie, 2006; Xu et al., 2015; Li et al., 2019; Zhang et al., 2019; Wang et al., 2020), while we focus on a lithologically-controlled fault network. Seismic-scale faults would cut through several layers in the vertical direction and communicate fluid between source rocks and reservoirs over a distance of several kilometers, e.g., San Andreas Parkfield (3 km, Rymer et al., 2006; Bradbury et al., 2011), EI Reno fault (1.6 km; Liao et al., 2019), Triunfo fault (0.2–0.6 km; Celestino et al., 2020) etc. These observations are probably limited in explaining lateral migration of hydrocarbon in a stratigraphic reservoir of ~hundred-meters in thickness. In this interpretation, the small scale conjugate fault networks have an optimal geometry in the brittle dolostone and might be expected to control the lateral migration and accumulation of subsurface fluid horizontally. However, the slip directions of the fault planes are difficult to determine based on the seismic attribute maps, which require supplementary data and fault-plane solutions.

5.3. Regional stresses and development of the fault networks

Large plate-scale regions are generally subjected to a uniform stress field (Engelder and Geiser, 1980; Zoback, 1992; Heidbach et al., 2010; Li

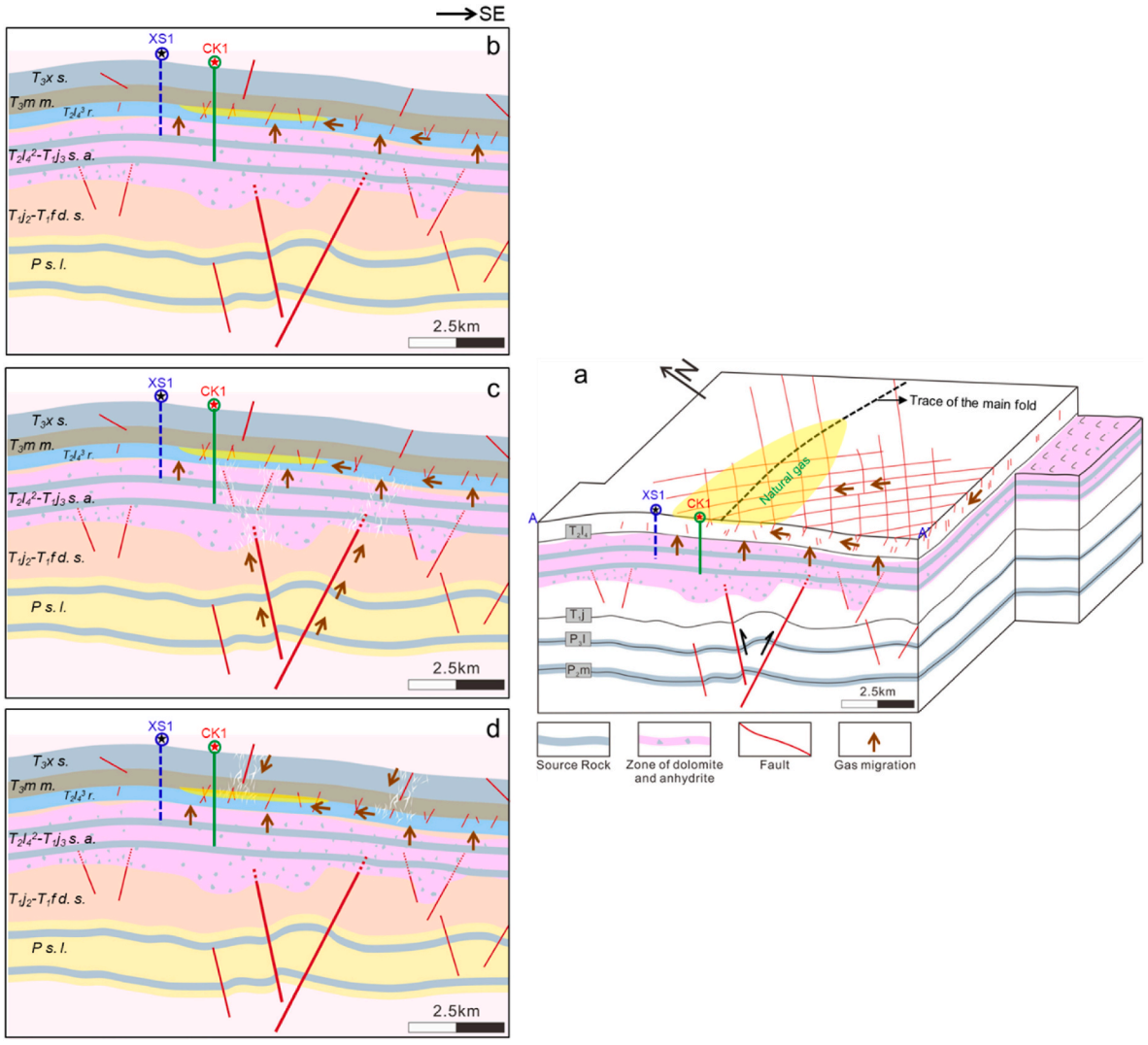

Fig. 7. (a) 3D hydrocarbon migration and accumulation models. The map displays: 1) structural interpretation map of the seismic profile A-A'; 2) motioning direction of the main faults; 3) location of main fold axis; 4) accumulation of natural gas; 5) drilling wells CK1 and XS1. (b–d) Three types of 2D hydrocarbon migration and accumulation models from the seismic profile (a) in Fig. 5. (b) Self-sourced migration and accumulation, (c) Long-range upward migration and accumulation, (d) Vertical downward migration and accumulation. Abbreviations: P s. l. (Permian Formation source rock and limestone); T_1j_2-T_1f d. s. (Lower Triassic Jia-2 member to Lower Triassic Feixianguan Formation dolostone and shale); $T_2l_4^2$-T_1j_3 s. a. (Middle Triassic Lei-4-2 submember to Lower Triassic Jia-3 Member source rock and anhydrite); $T_2l_4^3$ r. (Middle Triassic Lei-4-3 submember reservoir); T_3m m. (Upper Triassic Ma'anatng Formation mudstone); T_3x s. (Upper Triassic Xujiahe Formation source rock).

et al., 2016). As the eastern boundary of the Tibetan Plateau, the Longmen Shan is a steep transition zone between the Tibetan Plateau and the Sichuan Basin. The Longmen Shan has experienced several stages of rapid uplift with the latest and most important stage starting in the Late Miocene (Li et al., 2012; Dai et al., 2013; Wang et al., 2014). It is at this stage that Xinchang region is compressed and the Longquan Shan is uplifted as a response to the rapid uplift of the Longmen Shan about 10–15 Ma ago (Richardson et al., 2008; Li et al., 2012; Dai et al., 2013). Additionally, the direction of the maximum principle compressional stress of Longmen Shan and adjacent western Sichuan Basin was nearly on E-W during the Miocene-Pliocene, which is proximately parallel to the acute bisector of conjugate fault network in Figs. 3 and 4 (Burchfiel et al., 1995; Li et al., 2014). Faults tend to form within the brittle layer of dolostone while the weak/ductile layer of anhydrite can deform by distributed shearing and inflation that accommodate the overall strain (Davies et al., 2012; Ferrill et al., 2017a, 2017b, 2017b; Vasquez et al., 2018). The fault networks in the dolostone layer are more developed than underlaying anhydrite (Fig. S1), which we speculate is based on mechanical contrast that controls the lithologically-controlled conjugate faults. However, the primary fault network is not constrained by the lithologies.

6. Conclusions

Based on high-resolution 3D seismic data, we have interpreted fault networks in the Triassic Leikoupo Formation, composed of carbonates and evaporates, with implications for understanding gas migration and accumulation in carbonate reservoirs. We found that seismic attributes could be applied to identify the fault networks in the subsurface. The results show an orthogonal network of primary faults in the Xinchang region and a secondary set of conjugate fault networks in the fold limb. The observation of the conjugate fault networks integrated with fractures from core samples illustrates a lithologically-controlled conduit system for natural gas in the Leikoupo Formation. The characteristics of the conjugate fault networks favor the model of self-sourced migration and accumulation in the Xinchang reservoir, where the dolostone of the Leikoupo Formation, that contains such fault networks, as a potential exploration target.

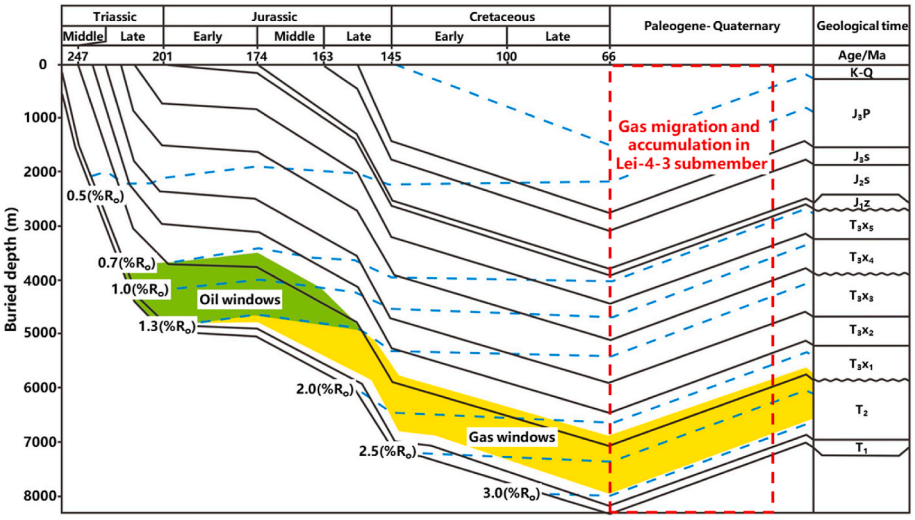

Fig. 8. A summary diagram showing the thermal evolution of organic matter in source rocks and hydrocarbon accumulation events at the CK1 well in the western Sichuan depression (modified after He et al., 2019). Abbreviations: T_1 (Lower Triassic); T_2 (Middle Triassic); T_3 (Upper Triassic); T_3x_1 (Member 1 of the Upper Triassic Xujiahe Formation); T_3x_2 (Member 2 of the Upper Triassic Xujiahe Formation); T_3x_3 (Member 3 of the Upper Triassic Xujiahe Formation); T_3x_4 (Member 4 of the Upper Triassic Xujiahe Formation); T_3x_5 (Member 5 of the Upper Triassic Xujiahe Formation); J_1z (Lower Jurassic Ziliujing Formation); J_2s (Middle Jurassic Shaximiao Formation); J_3s (Upper Jurassic Suining Formation); J_3p (Upper Jurassic Penglaizhen Formation); K-Q (Cretaceous to Quaternary); R_o (vitrinite reflectance).

Credit author statement

Lin Zhang: Methodology, Writing – original draft preparation; **Zonghu Liao:** Conceptualization, Writing and Supervision; **Ke Long:** Data curation and Software; **Brett M. Carpenter:** Writing – review & editing. **Huayao Zou:** Supervision and Validation; **Fang Hao:** Conceptualization.

Declaration of competing interest

The authors declare that they have no known competing financial interests or personal relationships that could have appeared to influence the work reported in this paper.

Acknowledgement

We thank Dr. Dancheng Zhu for the useful discussions. We acknowledge Sinopec for providing drilling cores and three-dimensional seismic survey used in this study. We are also grateful to three anonymous reviewers and JPSE editor Vural Sander Suicmez for helping to finalize the manuscript. This work was supported by Strategic Priority Research Program of the Chinese Academy of Sciences (No. XDA14010306) and National Key Research and Development Program of China (No. 2019YFC0605502). The authors declare no financial or other conflicts of interest.

Appendix A. Supplementary data

Supplementary data to this article can be found online at https://doi.org/10.1016/j.petrol.2021.109502.

References

Al-Dossary, S., Marfurt, K.J., 2006. 3d volumetric multispectral estimates of reflector curvature and rotation. Geophysics 71, P41–P51. https://doi.org/10.1190/1.2242449.

Ameen, M., 2003. Fracture and in-situ stress characterization of hydrocarbon reservoirs. Geo. Soc. London 209, 1–6. https://doi.org/10.1144/GSL.SP.2003.209.01.01.

Anders, M.H., Laubach, S.E., Scholz, C.H., 2014. Microfractures: a review. J. Struct. Geol. 69, 377–394. https://doi.org/10.1016/j.jsg.2014.05.011.

Bahorich, M., Farmer, S., 1995. 3-D seismic discontinuity for faults and stratigraphic features: the coherence cube. Lead. Edge 14 (10), 1053–1058. https://doi.org/10.1190/1.1437077.

Barchi, M.R., 2002. Lithological and structural controls on the seismogenesis of the Umbria Region: observations from seismic reflection profiles. Boll. Soc. Geol. Ital. 1, 855–864.

Bergbauer, S., Pollard, D.D., 2004. A new conceptual fold-fracture model including prefolding joints, based on the Emigrant Gap anticline, Wyoming. Geol. Soc. Am. Bull. 116 (3–4), 294–307. https://doi.org/10.1130/B25225.1.

Bhattacharya, S., Verma, S., 2019. Application of volumetric seismic attributes for complex fault network characterization on the North Slope, Alaska. J. Nat. Gas Sci. Eng. 65, 56–67. https://doi.org/10.1016/j.jngse.2019.02.002.

Billi, A., Salvini, F., Storti, F., 2003. The damage zone-fault core transition in carbonate rocks: implications for fault growth, structure and permeability. J. Struct. Geol. 25 (11), 1779–1794. https://doi.org/10.1016/S0191-8141(03)00037-3.

Bradbury, K.K., Evans, J.P., Chester, J.S., Chester, F.M., Kirschner, D.L., 2011. Lithology and internal structure of the San Andreas fault at depth based on characterization of Phase 3 whole-rock core in the San Andreas Fault Observatory at Depth (SAFOD) borehole. Earth Planet Sci. Lett. 310, 131–144. https://doi.org/10.1016/j.epsl.2011.07.020.

Burberry, C.M., Cannon, D.L., Cosgrove, J., Engelder, T., 2019. Fracture patterns associated with the evolution of the Teton anticline, Sawtooth Range, Montana, USA. Geological Society London Special Publications 487 (1). https://doi.org/10.1144/SP487.12.

Burchfiel, B.C., Chen, Z.L., Liu, Y.P., Royden, L.H., 1995. Tectonics of the Longmen Shan and adjacent regions, central China. Int. Geol. Rev. 37, 661–735. https://doi.org/10.1080/00206819509465424.

Caine, J.S., Evans, J.P., Forster, C.B., 1996. Fault zone architecture and permeability structure. Geology 24 (11), 1025–1028. https://doi.org/10.1130/0091-7613(1996)024<1025:FZAAPS>2.3.CO;2.

Carter, N., Lines, L., 2001. Fault imaging using edge detection and coherency measures on Hibernia 3-D seismic data. Lead. Edge 20 (1), 64–69. https://doi.org/10.1190/1.1438880.

Celestino, L., Alcione, M., Miranda, D., Siqueira, T., et al., 2020. Fault damage zones width: implications for the tectonic evolution of the northern border of the Araripe basin, Brazil, NE Brazil. J. Struct. Geol. 138 https://doi.org/10.1016/j.jsg.2020.104116.

Chen, Y.L., Zeng, Y., Duan, Y.M., Wang, Q.X., 2018. Pore structure characteristics and reservoir classification of dolomite reservoirs in fourth member of Leikoupo Formation, Longmen Mountain front, western Sichuan Basin. Petroleum Geology and Experiment 40 (5), 621–631 (in Chinese).

Chester, F.M., Chester, J.S., 1998. Ultracataclasite structure and friction processes of the Punchbowl fault, San Andreas system, California. Tectonophysics 295, 199–221. https://doi.org/10.1016/S0040-1951(98)00121-8.

Chester, F.M., Evans, J.P., Biegel, R.L., 1993. Internal structure and weakening mechanisms of the San Andreas fault. J. Geophys. Res. 98, 771–786. https://doi.org/10.1029/92JB01866.

Chilingarian, G.V., Mazzullo, S.J., Reike, H.H., 1992. Carbonate Reservoir Characterization: A Geological-Engineering Analysis: Part I: Amsterdam. Elsevier Science Publishers BV, p. 640.

Chopra, S., Marfurt, K.J., 2007. Seismic attributes for prospect identification and reservoir characterization. SEG, Geophysical Developments Series 11.

Crider, J.G., Peacock, D.C.P., 2004. Initiation of brittle faults in the upper crust: a review of field observations. J. Struct. Geol. 26 (4), 691–707. https://doi.org/10.1016/j.jsg.2003.07.007.

Dai, J.G., Wang, C.S., Hourigan, J., Santosh, M., 2013. Insights into the early Tibetan Plateau from (U-Th)/He thermochronology. J. Geol. Soc. London 170, 917–927. https://doi.org/10.1144/jgs2012-076.

Dai, J.X., Yu, C., Huang, S.P., Gong, D.Y., Wu, W., Fang, C.C., Liu, D., 2014. Geological and geochemical characteristics of large gas fields in China. Petrol. Explor. Dev. 41 (1), 1–13 (in Chinese).

Davies, R.K., Knipe, R.J., Welch, M.J., 2012. The role of vertical mechanical heterogeneity in predicting fault zone architecture. In: 3rd European Association of Geoscientists & Engineers International Conference on Fault and Top Seals. Abstract P24.

De Paola, N., Collettini, C., Faulkner, D., Trippetta, F., 2008. Fault zone architecture and deformation processes within evaporitic rocks in the upper crust. Tectonics 27 (4), TC4017. https://doi.org/10.1029/2007TC002230.
Ellsworth, W.L., 2013. Injection-induced earthquakes. Science 341 (6142), 1225942. https://doi.org/10.1126/science.1225942.
Eng, C., Tsuji, T., 2019. Influence of faults and slumping on hydrocarbon migration inferred from 3D seismic attributes: sanriku-Oki forearc basin, northeast Japan. Mar. Petrol. Geol. 99, 175–189. https://doi.org/10.1016/j.marpetgeo.2018.10.013.
Engelder, T., Geiser, P., 1980. On the use of regional joint sets as trajectories of paleostress fields during the development of the Appalachian Plateau, New York. J. Geophys. Res. 85 (B11), 6319–6341. https://doi.org/10.1029/JB085iB11p06319.
Ferrill, D.A., Evans, M.A., McGinnis, R.N., Morris, A.P., Smart, K.J., Wigginton, S.S., Gulliver, K.D.H., Lehrmann, D., de Zoeten, E., Sickmann, Z., 2017a. Fault zone processes in mechanically layered mudrock and chalk. J. Struct. Geol. 97, 118–143. https://doi.org/10.1016/j.jsg.2017.02.013.
Ferrill, D.A., Morris, A.P., McGinnis, R.N., Smart, K.J., Wigginton, S.S., Hill, N.J., 2017b. Mechanical stratigraphy and normal faulting. J. Struct. Geol. 94, 275–302. https://doi.org/10.1016/j.jsg.2016.11.010.
Flodin, E., Aydin, A., 2004. Evolution of a strike-slip fault network,Valley of fire state Park, southern Nevada. Geol. Soc. Am. Bull. 116 (1–2), 42–59. https://doi.org/10.1130/B25282.1.
Gao, D.L., 2013. Integrating 3D seismic curvature and curvature gradient attributes for fracture characterization: methodologies and interpretational implications. Geophysics 78 (2), O21–O31. https://doi.org/10.1190/GEO2012-0190.1.
Ghosh, K., Mitra, S., 2009. Structural controls of fracture orientations, intensity, and connectivity, Teton anticline, Sawtooth Range, Montana. AAPG Bull. 93 (8), 995–1014. https://doi.org/10.1306/04020908115.
Guo, J.L., Gao, S., Wu, Y.B., Li, M., Chen, K., Hu, Z.C., Chen, H.H., 2014. 3.45 Ga granitic gneisses from the yangtze craton, south China: implications for early archean crustal growth. Precambrian Res. 242, 82–95. https://doi.org/10.1016/j.precamres.2013.12.018.
He, D.F., Ma, Y.S., Li, Y.Q., Wu, S.L., 2019. New directions in an established gas play: promising dolomite reservoirs in the middle triassic Leikoupo Formation of the Sichuan Basin, China. AAPG Bull. 103 (1) https://doi.org/10.1306/05111816502.
Heidbach, O., Tingay, M., Barth, A., Reinecker, J., Kurfeß, D., Müller, B., 2010. Global crustal stress pattern based on the World Stress Map database release 2008. Tectonophysics 482 (1–4), 3–15. https://doi.org/10.1016/j.tecto.2009.07.023.
Iacopini, D., Butler, R.W.H., 2011. Imaging deformation in submarine thrust belts using seismic attributes. Earth Planet Sci. Lett. 302 (3–4), 414–422. https://doi.org/10.1016/j.epsl.2010.12.041.
Karlsen, D.A., Skeie, J.E., 2006. Petroleum migration, faults and overpressure: calibrating basin modeling using petroleum in traps-a review. J. Petrol. Geol. 29 (3), 227–256. https://doi.org/10.1111/j.1747-5457.2006.00227.x.
Kim, Y.S., Peacock, D.C.P., Sanderson, D.J., 2003. Mesoscale strike-slip faults and damage zones at Marsalforn, Gozo Island, Malta. J. Struct. Geol. 25, 793–812. https://doi.org/10.1016/S0191-8141(02)00200-6.
Laubach, S.E., 2003. Practical approaches to identifying sealed and open fractures. AAPG Bull. 87 (4), 561–579. https://doi.org/10.1306/11060201106.
Li, Y., Zeng, Y., Yi, H., 1995. Sedimentary and Tectonic Evolution of the Longmen Shan Foreland Basin, Western Sichuan. Chengdu: Press of Chengdu University of Science and Technology, China, pp. 1–92 (in Chinese).
Li, Y., Allen, P.A., Densmore, A.L., Qiang, X., 2003. Evolution of the longmen Shan foreland basin (western sichuan, China) during the late triassic indosinian orogeny. Basin Res. 15 (1), 117–138. https://doi.org/10.1046/j.1365-2117.2003.00197.x.
Li, Z.W., Liu, S.G., Chen, H.D., Deng, B., 2012. Spatial variation in Meso-Cenozoic exhumation history of the Longmen Shan thrust belt (eastern Tibetan Plateau) and the adjacent western Sichuan basin: constraints from fission track thermochronology. J. Asian Earth Sci. 47, 185–203. https://doi.org/10.1016/j.jseaes.2011.10.016.
Li, Z., Jia, D., Chen, W., Yin, H., Shen, L., Sun, C., Zhang, Y., Li, Y., Li, S., Zhou, X., Li, H., Jian, G., Zhang, M., Cui, J., 2014. Late Cenozoic east-west crustal shortening in southern Longmen Shan, eastern Tibet: implications for regional stress field changes. Tectonophysics 623, 169–186. https://doi.org/10.1038/s41598-020-77634-6.
Li, P., Hao, F., Guo, X., Zou, H., Yu, X., Wang, G., 2015. Processes involved in the origin and accumulation of hydrocarbon gases in the Yuanba gas field, Sichuan Basin, southwest China. Mar. Petrol. Geol. 59, 150–165. https://doi.org/10.1016/j.marpetgeo.2014.08.003.
Li, Z.G., Zeng, J.L., Jia, D., Sun, C., Wang, W., Yuan, Z.D., Liu, B.J., 2016. Quaternary activity of the Range Front thrust system in the Longmen Shan piedmont, China, revealed by seismic imaging and growth strata. Tectonics 35, 2807–2827. https://doi.org/10.1002/2015TC004093.
Li, M., Wu, G., Xia, B., Huang, T., Ni, B., Pang, S., Long, X., 2019. Controls on hydrocarbon accumulation in clastic reservoirs of the Tarim Craton, NW China. Mar. Petrol. Geol. 104, 423–437. https://doi.org/10.1016/j.marpetgeo.2019.04.008.
Liao, Z., Liu, H., Jiang, Z., 2017. Fault damage zone at subsurface: a case study using 3D seismic attributes and a clay model analog for the Anadarko Basin. Oklahoma. Interpretation 5 (2), 141–150. https://doi.org/10.1190/INT-2016-0033.1.
Liao, Z., Liu, H., Carpenter, B.M., Marfurt, K.J., Reches, Z., 2019. Analysis of fault damage zones using three-dimensional seismic coherence in the Anadarko Basin, Oklahoma. AAPG Bull. 103 (8), 1771–1785. https://doi.org/10.1306/1219181413417207.
Liu, S.H., Jin, X.B., Hu, Y.Z., Yang, Z.B., 2010. Exploration prospect of lower Triassic in western Sichuan basin: an application of Chuanke 1 well. Nat. Gas Explor. Dev+. 4, 21–24 (in Chinese with English abstract).
Long, K., Chen, Z.Y., Song, X.B., Yuan, H., 2019. Analysis on natural gas source of middle triassic Leikoupo Formation in western Sichuan Basin, China. Nat. Gas. Ind. S1, 48–53 (in Chinese).
Lu, R., He, D., Xu, X., Tan, X., Li, Y., Cai, M., Wang, Z., 2019. Geometry and kinematics of buried structures in the piedmont of the central Longmen Shan: implication for the growth of the Eastern Tibetan Plateau. J. Geol. Soc. London 176 (2), 323–333. https://doi.org/10.1144/jgs2018-015.
Lunn, R.J., Willson, J.P., Shipton, Z.K., Moir, H., 2008. Simulating brittle fault growth from linkage of preexisting structures. J. Geophys. Res. 113 (B7), B07403. https://doi.org/10.1029/2007JB005388.
Luo, Y., Higgs, W.G., Kowalik, W.S., 1996. Edge detection and stratigraphic analysis using 3D seismic data. SEG Tech. Progr. Expand. Abstr. https://doi.org/10.1190/1.1826632.
Luo, Y., Wang, Y., Liu, H., Wang, G., Zhao, Y., 2020. Overpressure controlling factors for tectonic fractures in near-source tight reservoirs in the southwest Ordos Basin, China. J. Petrol. Sci. Eng. 188, 106818. https://doi.org/10.1016/j.
Maher Jr., Harmon D.. Structural mini-atlas for physical geology lecture [EB/OL], 2019-09. http://maps.unomaha.edu/Maher/geo117/part3/structures/structureatlas.html.
Marfurt, K.J., Kirlin, R.L., Farmer, S.L., Bahorich, M.S., 1998. 3-D seismic attributes using a semblance based coherency algorithm. Geophysics 63, 1150–1165. https://doi.org/10.1190/1.1444415.
Marfurt, K.J., Sudhaker, V., Gersztenkorn, A., Crawford, K.D., Nissen, S.E., 1999. Coherency calculations in the presence of structural dip. Geophysics 64, 104–111. https://doi.org/10.1190/1.1444508.
Miller, S.A., Collettini, C., Chiaraluce, L., Cocco, M., Barchi, M., Kaus, B., 2004. Aftershocks driven by a high-pressure CO2 source at depth. Nature 27, 724–727. https://doi.org/10.1038/nature02251.
Nixon, C.W., Sanderson, D.J., Dee, S.J., Bull, J.M., Humphreys, R.J., Swanson, M.H., 2014. Fault interactions and reactivation within a normal-fault network at Milne Point, Alaska. AAPG Bull. 98 (10), 2081–2107. https://doi.org/10.1306/04301413177.
Putz-Perrier, M.W., Sanderson, D.J., 2010. Distribution of faults and extensional strain in fractured carbonates of the North Malta Graben. AAPG Bull. 94 (4), 435–456. https://doi.org/10.1306/08260909063.
Richardson, N.J., Densmore, A.L., Seward, D., Fowler, A., Wipf, M., Ellis, M.A., Li, Y., Zhang, Y., 2008. Extraordinary denudation in the Sichuan Basin: insights from low-temperature thermochronology adjacent to the eastern margin of the Tibetan Plateau. J. Geophys. Res. 113 (B4), B04409 https://doi.org/10.1029/2006JB004739.
Roberts, A., 2001. Curvature attributes and their application to 3d interpreted horizons. First Break 19, 85–100.
Rymer, M.J., Hickman, S.H., Stoffer, P.W., 2006. A field guide to the central, creeping section of the san Andreas fault and the san Andreas fault observatory at depth. In: Prentice, C.S., Scotchmoor, J.G., Moores, E.M., Kiland, J.P. (Eds.), 1906. San Francisco Earthquake Centennial Field Guides: Field Trips Associated with the 100th Anniversary Conference, 18-23 April, vol. 7. Geological Society of America Field Guide, San Francisco, California, pp. 237–272.
Sarkar, S., Marfurt, K.J., Slatt, R.M., 2010. Generation of sea-level curves from the depositional pattern as seen through seismic attributes-seismic geomorphology analysis of an MTC-rich shallow sediment column, northern Gulf of Mexico. Lead. Edge 29 (9), 1084–1091. https://doi.org/10.1190/1.3485769.
Segall, P., Paola, D.D., 1983. Nucleation and growth of strike slip faults in granite. J. Geophys. Res. 88 (B1), 555. https://doi.org/10.1029/JB088iB01p00555.
Stearns, D.W., 1968. Certain aspects of fracture in naturally deformed rocks. In: Reicker, R.E. (Ed.), Advanced Science Seminar in Rock Mechanics. Air Force Cambridge Research Laboratory, Bedford, MA, pp. 97–118.
Sun, T.G., Luo, X.P., Qing, H.R., 2020. Characteristics and natural gas origin of Middle–Late triassic marine source rocks of the western sichuan depression, SW China. Acta Geol. Sin. 94 (2), 376–398. https://doi.org/10.1111/1755-6724.14341.
Tian, H., Tang, S., Zhang, J.Y., Xin, Y.G., Wang, X., Li, W.Z., 2018. Characteristics and formation conditions of carbonate reservoir in Leikoupo Formation of western Sichuan Basin. Nat. Gas Geosci. 29 (11), 1585–1594 (in Chinese).
Vasquez, L., Nalpas, T., Ballard, J.F., Le Carlier De Veslud, C., Simon, B., Dauteuil, O., Bernard, X.D., 2018. 3D geometries of normal faults in a brittle-ductile sedimentary cover: analogue modelling. J. Struct. Geol. 112, 29–38. https://doi.org/10.1016/j.jsg.2018.04.009.
Wang, C.S., Dai, J.G., Zhao, X.X., Li, Y.L., Graham, S.A., He, D.F., Ran, B., Meng, Jun, 2014. Outward-growth of the Tibetan plateau during the cenozoic: a review. Tectonophysics 621, 1–43. https://doi.org/10.1016/j.tecto.2014.01.036.
Wang, X.J., Yang, Z.R., Han, B., 2015. Superposed evolution of Sichuan Basin and its petroleum accumulation. Front. Earth Sci. 22 (3), 161–173 (in Chinese).
Wang, F., Chen, D., Wang, Q., Shi, X., Xie, G., Wang, Z., Li, J., Liao, W., 2020. Evolution characteristics of transtensional faults and their impacts on hydrocarbon migration and accumulation: a case study from the Huimin Depression, Bohai Bay Basin, eastern China. Mar. Petrol. Geol. 120 https://doi.org/10.1016/j.marpetgeo.2020.104507.
Watkins, H., Butler, R.W., Bond, C.E., Healy, D., 2015. Influence of structural position on fracture networks in the Torridon Group, Achnashellach fold and thrust belt, NW Scotland. J. Struct. Geol. 74, 64–80. https://doi.org/10.1016/j.jsg.2015.03.001.
Applications of 3-D seismic data to exploration and production. In: Weimer, P., Davis, T. L. (Eds.), 1996. AAPG Studies in Geology 42, vol. 5. SEG Geophysical Developments Series, p. 276.
Wilson, T.H., Smith, V., Brown, A., 2015. Developing a model discrete fracture network, drilling, and enhanced oil recovery strategy in an unconventional naturally fractured

reservoir using integrated field, image log, and three-dimensional seismic data. AAPG Bull. 99 (4), 735–762. https://doi.org/10.1306/10031414015.

Wu, X., 2017. Directional structure-tensor-based coherence to detect seismic faults and channels. Geophysics 82, A13–A17. https://doi.org/10.1190/GEO2016-0473.1.

Xiao, K., Li, H., Duan, Y., Zhang, Y., Liu, L., 2019. Reservoir characteristics and main controlling factors of the Leikoupo gas pools in the western Sichuan Basin. Nat. Gas. Ind. 39 (6), 34–44 (in Chinese).

Xie, G.P., 2015. Source of gas reservoirs in the fourth member of the middle triassic Leikoupo Formation in western sichuan depression. Petroleum Geology and Experiment 37 (4), 418–422 (in Chinese with English abstract).

Xu, G.M., Feng, X., Zhu, L., Wang, Q.X., 2011. Exploration suggestions on Leikoupo to maantang formations in Xinchang structural belt, west Sichuan Basin. Natural Gas Technology and Economy 5 (5), 16–21 (in Chinese with English abstract).

Xu, G.M., Song, X.B., Feng, X., Long, K., Wang, Q.X., Shi, G.S., Zhu, L., 2013. Gas potential of the middle triassic Leikoupo Formation in the western Sichuan Basin. Nat. Gas. Ind. 33 (8), 8–14 (in Chinese with English abstract).

Xu, S., Hao, F., Xu, C., Wang, Y., Zou, H., Gong, C., 2015. Differential compaction faults and their implications for fluid expulsion in the northern Bozhong Subbasin, Bohai Bay Basin, China. Mar. Petrol. Geol. 63, 1–16. https://doi.org/10.1016/j.marpetgeo.2015.02.013.

Yang, K.M., 2016. Hydrocarbon potential of source rocks in the middle triassic Leikoupo Formation in the western sichuan depression. Petroleum Geology and Experiment 38 (3), 366–374 (in Chinese).

Zhang, S.B., Zheng, Y.F., 2013. Formation and evolution of Precambrian continental lithosphere in South China. Gondwana Res. 23, 1241–1260. https://doi.org/10.1016/j.gr.2012.09.005.

Zhang, J., Cao, J., Wang, Y., Hu, G., Zhou, N., Shi, T., 2019. Origin of giant vein-type bitumen deposits in the northwestern Junggar Basin, NW China: implications for fault-controlled hydrocarbon accumulation. J. Asian Earth Sci. 179, 287–299. https://doi.org/10.1016/j.jseaes.2019.05.009.

Zoback, M.L., 1992. First- and second-order patterns of stress in the lithosphere: the world stress map project. J. Geophys. Res. 97 (B8), 11703–11728. https://doi.org/10.1029/92JB00132.